

Trigger mechanism for a singing cavitating tip vortex

Zhaohui Qian^{1,2}, Yongshun Zeng^{1,2}, Xiaoxing Peng³ and Xianwu Luo^{1,2,†}

¹Beijing Key Laboratory of CO₂ Utilization and Reduction Technology, Department of Energy and Power Engineering, Tsinghua University, Beijing 100084, China;

²State Key Laboratory of Hydro-science and Engineering, Tsinghua University, Beijing 100084, China;

³National Key Lab on Ship Vibration and Noise, China Ship Scientific Research Center, Wuxi 214082, China;

† Email address for correspondence: luoxw@tsinghua.edu.cn

The discrete tone radiated from tip vortex cavitation (TVC), known as ‘vortex singing’, was recognized in 1989, but its triggering remains unclear for over thirty years. In this study, the desinent cavitation number and viscous correction are applied to describe the dynamics of cavitation bubbles and the dispersion relation of cavity interfacial waves. The wavenumber-frequency spectrum of the cavity radius from the experiment in *CSSRC* indicates that singing waves predominantly consist of the stationary double helical modes ($k_\theta = 2^-$ and -2^+) and the breathing mode ($k_\theta = 0^-$), rather than standing waves as assumed in previous literatures. Moreover, two trigger mechanisms, expressed by two triggering lines, are proposed: the twisted TVC, initially at rest, is driven into motion through the corrected natural frequency (f_n) due to the step change of the far-field pressure. Subsequently, the frequency associated with the zero-group-velocity point (f_{zgv}) at $k_\theta = 0^-$ is excited through f_i , the frequency at the intersection of dispersion curves at $k_\theta = 0^-$ and -2^+ , or f_j , the frequency at the intersection of dispersion curves at $k_\theta = 0^-$ and 2^- , corresponding to two types of the vortex singing triggering. These solutions, without empirical parameters, are validated using singing conditions provided by *CSSRC* and *G.T.H.*, respectively. Furthermore, the coherence and the cross-power spectral density spectrum indicates a large-scale breathing wave propagating along the singing cavity surface and travelling from downstream to hydrofoil tip, providing us a comprehensive understanding for the triggering of vortex singing.

Key words: vortex singing, trigger mechanism, cavity dynamics, interfacial wave

1. Introduction

Cavitation has been an attractive topic in the field of hydraulic machinery and ocean engineering for over one hundred years (Arndt *et al.* 1991; Brennen 2014; Luo *et al.* 2022). Among various types of cavitation, the tip vortex cavitation (TVC) is the first one to appear on propellers or axial-flow turbines, acting as a crucial source for underwater noise and vibrations (Posa *et al.* 2022; Qian *et al.* 2022; Ji *et al.* 2023). Consequently, many studies focused on forecasting TVC’s inception (Arndt & Keller

1992; Amini *et al.* 2019; Chen *et al.* 2019), capturing general features such as the vortex trajectory, vapor core radius and roll-up kinematics (Asnaghi *et al.* 2020; Xie *et al.* 2021; Cheng *et al.* 2021; Russell *et al.* 2023), with few discussions concerning the cavity dynamics and noise generation mechanisms (Pennings *et al.* 2016a; Liu & Wang 2019; Klapwijk *et al.* 2022; Wang *et al.* 2023).

A representative noise enhancement phenomenon, excited by the TVC's interfacial instability, is the emission of a relatively higher amplitude and discrete tone from the fully developed TVC under certain operation conditions, which was firstly reported by Higuchi (1989) and named as 'vortex singing' by Maines & Arndt (1997). They tested different hydrofoils by varying the velocity, angle of attack and water quality in two facilities, one in *Obernach*, Germany and one at St. Anthony Falls Laboratory (*SAFL*), USA. The vortex singing was triggered within a distinct range of singing cavitation number, σ_s , and the standing wave along the cavity surface appeared to oscillate in phase with the sheet cavity at the tip. Furthermore, the singing frequency, f_s , typically changes from 400 Hz to 1.1 kHz and induces an intense peak of 20 dB to 30dB above the background in the noise spectrum (Arndt *et al.* 2015). Briançon-Marjollet and Merle (1996) described their observations on the singing vortex over the hydrofoil with a NACA 0020 cross-section in a larger cavitation tunnel, G.T.H., however the available conditions deviated from the narrow range of both σ_s and f_s defined for singing points by *SAFL* and *Obernach*.

One of the elliptical foil geometries, with NACA 662-415 section, was tested in *Delft* University of Technology by Pennings *et al.* (2015a). Although the vortex singing did not appear in the experiment, the property of TVC dynamics agrees well with that in *SAFL* and *Obernach*. The same foil has been tested in a smaller cavitation tunnel, *CSSRC*, by Peng *et al.* (2017a). They developed a reliable experiment process to trigger the vortex singing by varying the cavitation number, σ , with a step change until it approaches σ_s . Song *et al.* (2018) also regenerated the TVC-singing in *CSSRC* and further pointed out that the inflow dissolved gas (D_o) imposed a significant and similar effect on both the singing cavitation number, σ_s , and the desinent cavitation number, σ_d . Recently, Ye *et al.* (2021, 2023) found the travelling of breathing waves along the TVC at Zhejiang University (*ZJU*), similar to the travelling waves of vortex singing at *CSSRC*. However, no vortex singing could be heard. Due to the higher dissolved gas content and σ_d in their experiments, it could be inferred that the vortex singing is sensitive to the distance between σ and σ_d . Because the triggering theories of vortex singing remains unclear, neither experiment nor numerical simulation can accurately excite the intense cavity resonance and the discrete emitted noise from a developed TVC (Simanto *et al.* 2023; Klapwijk *et al.* 2022).

To find the trigger mechanism for a vortex singing from TVC, two-dimensional (2-D) cavitation bubble kinematics and dynamics were examined theoretically and numerically (Choi & Ceccio 2007; Choi *et al.* 2009; Bosschers 2018a). The self-excited frequency f_n , known as the natural oscillation frequency, seems to be a primary resonance source for the singing frequency f_s . However, the 2-D analytical prediction with acceptable accuracy for f_n becomes extremely challenging (Bosschers 2009b). Therefore, the three-dimensional (3-D) dispersion relation was further applied

to solve the f_n . As suggested by Keller & Escudier (1980), the standing wave is possibly generated if the vortex is superimposed on the uniform axial flow. Using this idea, Maines & Arndt (1997) explained the determination of σ_s and f_s in *SAFL* and *Obernach*, but the agreement between their results and that in *G.T.H.* is poor and not acceptable. The dispersion relation for predicting deformations over a TVC was proposed by Pennings *et al.* (2015a, 2015b), applying the *Lamb-Oseen* vortex model. Based on the same consideration, Bosschers (2009a) introduced the semi-empirical viscous correction and left the criterion of zero-group-velocity point on breathing waves as the most likely hypothesis for stimulating f_s , with other criteria, for instance, the crossing points of dispersion lines for breathing waves and double helical waves (Bosschers 2018a). The main issue with his model is its inability to predict σ_s for vortex singing (Pennings *et al.* 2015b). Furthermore, it also fails to interpret the absence of singing signal in *Delft* and *ZJU* (Bosschers 2018b).

On the other hand, Peng *et al.* (2017a) emphasized that vortex singing requires a closed sheet cavity at the tip and a twisted shape of the column cavity before singing. This suggests that either a helical mode wave is involved or there is an interaction between the sheet cavity and breathing waves propagating along TVC with the negative phase velocity at the zero-group-velocity condition. Determining these mechanisms requires more analysis of the dispersion relation in viscous flows.

In the exploration of vortex singing over the past thirty years, the greatest obstacle for both experiment and numerical simulation is the unclear triggering theory (Arndt 2002). Therefore, in this paper, the 2-D and 3-D resonance frequencies for TVC are proposed. Furthermore, the viscous corrections and analytical triggering criteria are given to explain how and where the TVC's singing should be triggered.

2. Theoretical analysis

2.1. Resonance frequency of a vortex cavity in 2-D viscous flow

In the study of resonance frequency for a vortex cavity in 2D viscous flow, the far-end of the TVC exhibits a fully developed interface, which can be characterized as a 2D axisymmetric cavitation bubble. Under isothermal conditions, the pressure within the bubble, p_v , is assumed constant. As the radius, R , of bubble increases, the bubble's wall displaces the surrounding liquid from the axis, leading to a decrease in tangential velocity due to the conservation of angular momentum and an increase of the local pressure, which resists the further inflation. Conversely, decreasing R results in the increased tangential velocity and the decreased local pressure, preventing the bubble from collapsing. The associated resonance frequency, f_n , also known as the natural frequency of TVC is formulated as (Franc & Michel, 2016),

$$f_n = \frac{U_\infty}{2\pi r_c} \sqrt{\sigma K_\sigma / \ln \frac{r_\infty}{r_c}} \quad (2.1)$$

where r_∞ is the distance from the tunnel's wall to the vortex axis, and $r_\infty \gg R$ should be satisfied to ensure minimal impact on far-field pressure, p_∞ . Here, r_c represents the equilibrium radius, σ is the far-field cavitation number, which is defined by $(p_\infty - p_v) / (0.5\rho_L U_\infty^2)$, with ρ_L and U_∞ denoting the density and velocity of the liquid. K_σ means

the tangential stiffness coefficient.

The 2-D cavitation bubble oscillation is initially considered as the most probable resonance source of the vortex singing, because f_n is triggered by the step change of the far field pressure but not affected by the step time (Bosschers 2018b), therefore, accurate prediction of f_n using Equation (2.1) is crucial. Conventional methods use $K_\sigma = 1.0$ (Franc & Michel 2016) but overpredict the singing frequency due to the neglect of viscous effects (Bosschers 2009b). Determining K_σ for a viscous cavitating vortex remains a challenge. In this paper, a new linearization strategy is physically proposed to resolve f_n .

Under the conditions of incompressible, zero mass transport across the bubble wall, neglecting the surface tension and non-condensable gas, the fluid velocity u and pressure p are determined by,

$$\frac{1}{r}(R\ddot{R} + \dot{R}^2 - \frac{1}{r^2}R^2\dot{R}^2 - u_\theta^2) = -\frac{1}{\rho_L} \frac{\partial p}{\partial r} \quad (2.2)$$

where R , \dot{R} and \ddot{R} are the radius, velocity and acceleration of bubble wall.

For the equilibrium condition, $\dot{R} = 0$ and $\ddot{R} = 0$, the Equation (2.2) is rewritten in the simplified form as,

$$-u_\theta^2 / r = -\frac{1}{\rho_L} \frac{\partial p}{\partial r} \quad (2.3)$$

and in steady state, the azimuthal velocity u_θ follows the *Lamb-Oseen* vortex profile,

$$u_\theta(r) = \frac{\Gamma_\infty}{2\pi r} (1 - e^{-a(r/r_{cv})^2}) \quad (2.4)$$

which Γ_∞ is the circulation, r_{cv} denotes the viscous core radius, and $a = 1.2564$ helps u_θ to reach its peak at $r = r_{cv}$. Even though the *Lamb-Oseen* model does not precisely model the azimuthal velocity due to the lack of coupling with axial flows, it properly accounts for viscosity effects (Pennings 2016b). By integrating u_θ from bubble wall to far-field in the radial direction, the Equation (2.3) becomes,

$$\int_{r_c}^{r_\infty} \left\{ \left[\frac{\Gamma_\infty}{2\pi r} (1 - e^{-a(r/r_{cv})^2}) \right]^2 / r \right\} dr = \int_{r_c}^{r_\infty} \left(\frac{1}{\rho_L} \frac{\partial p}{\partial r} \right) dr \quad (2.5)$$

where the boundary condition $p(r = r_c) = p_v$ is used to solve the Equation (2.5),

$$\begin{aligned} & \frac{\rho_L \Gamma_\infty^2}{8\pi^2 r_{cv}^2} \left\{ -\frac{r_c^2}{r_\infty^2} - \frac{r_{cv}^2}{r_\infty^2} e^{-2a(r_\infty/r_{cv})^2} + \frac{2r_{cv}^2}{r_\infty^2} e^{-a(r_\infty/r_{cv})^2} - 2aEi[-2a(r_\infty/r_{cv})^2] + 2aEi[-a(r_\infty/r_{cv})^2] \right. \\ & \left. + \frac{r_c^2}{r_c^2} + \frac{r_{cv}^2}{r_c^2} e^{-2a(r_c/r_{cv})^2} - 2\frac{r_{cv}^2}{r_c^2} e^{-a(r_c/r_{cv})^2} + 2aEi[-2a(r_c/r_{cv})^2] - 2aEi[-a(r_c/r_{cv})^2] \right\} \\ & = p_\infty - p_v = \frac{1}{2} \rho_L U_\infty^2 \sigma \end{aligned} \quad (2.6)$$

with Ei corresponding to the exponential integral function.

Linearizing r_c relative to r_{cv} with a parameter k_c , i.e. $r_c = k_c r_{cv}$, the circulation, Γ_∞ , is

derived from the Equation (2.6) by assuming $r_\infty \gg r_{cv}$,

$$\Gamma_\infty^2 \approx \frac{4\pi^2 r_c^2 U_\infty^2 \sigma}{1 + e^{-2ak_c^2} - 2e^{-ak_c^2} + 2ak_c^2 Ei(-2ak_c^2) - 2ak_c^2 Ei(-ak_c^2)} \quad (2.7)$$

To describe the cavity oscillation dynamics, the Equation (2.2) with unsteady terms is solved using the time-varying vortex core radius r_v , substituting the Equation (2.4) into the Equation (2.2) and then integrating from R to r_∞ in the radial direction induces the equation,

$$R\ddot{R} \ln \frac{r_\infty}{R} + \dot{R}^2 \ln \frac{r_\infty}{R} + \frac{1}{2} R^2 \dot{R}^2 \left(\frac{1}{r_\infty^2} - \frac{1}{R^2} \right) - \int_R^{r_\infty} \frac{\Gamma_\infty^2}{4\pi^2 r^3} (1 - e^{-a(r/r_v)^2})^2 dr = -\frac{p_\infty - p(R)}{\rho_L} \quad (2.8)$$

where the pressure on the bubble wall is calculated by,

$$p(R) = p_v - 2\mu_L \frac{\dot{R}}{R} \quad (2.9)$$

here μ_L denotes the molecular viscosity of liquid. For small-amplitude oscillations, by the radial oscillation coefficient $k(t)$, $R = kr_{cv}$ is utilized to rewrite the Equation (2.8),

$$\begin{aligned} & \ddot{k} + \frac{2\nu_L}{r_{cv}^2 k^2 \ln \frac{r_\infty}{kr_{cv}}} \dot{k} + \left(\frac{1}{k} + \frac{r_{cv}^2}{2r_\infty^2} \frac{k}{\ln \frac{r_\infty}{kr_{cv}}} - \frac{1}{2k \ln \frac{r_\infty}{kr_{cv}}} \right) k^2 \\ & + \frac{\Gamma_\infty^2}{8\pi^2 r_{cv}^4} \left\{ \frac{r_{cv}^2}{r_\infty^2} \frac{1}{k \ln \frac{r_\infty}{kr_{cv}}} + \frac{r_{cv}^2}{r_\infty^2} \frac{e^{-2a(r_\infty/r_v)^2}}{k \ln \frac{r_\infty}{kr_{cv}}} - \frac{2r_{cv}^2}{r_\infty^2} \frac{e^{-a(r_\infty/r_v)^2}}{k \ln \frac{r_\infty}{kr_{cv}}} + \frac{2aEi[-2a(r_\infty/r_v)^2]}{k \ln \frac{r_\infty}{kr_{cv}}} - \frac{2aEi[-a(r_\infty/r_v)^2]}{k \ln \frac{r_\infty}{kr_{cv}}} \right. \\ & \left. - \frac{2aEi[-2ak^2(r_{cv}/r_v)^2]}{k \ln \frac{r_\infty}{kr_{cv}}} + \frac{2aEi[-ak^2(r_{cv}/r_v)^2]}{k \ln \frac{r_\infty}{kr_{cv}}} - \frac{1}{k^3 \ln \frac{r_\infty}{kr_{cv}}} - \frac{e^{-2ak^2(r_{cv}/r_v)^2}}{k^3 \ln \frac{r_\infty}{kr_{cv}}} + \frac{2e^{-ak^2(r_{cv}/r_v)^2}}{k^3 \ln \frac{r_\infty}{kr_{cv}}} \right\} = -\frac{(p_\infty - p_v)}{\rho_L r_{cv}^2 k \ln \frac{r_\infty}{kr_{cv}}} \end{aligned} \quad (2.10)$$

According to Choi *et al.* (2009), k is assumed as constant when the singing cavity occurs with small-scale oscillations to linearize the Equation (2.10), i.e.

$$\frac{R}{r_v} = \frac{kr_{cv}}{r_v} \approx \frac{r_c}{r_{cv}} = k_c \quad (2.11)$$

By eliminating the nonlinear and high-order terms, and incorporating the Equation (2.6), the Equation (2.10) is simplified to a standard second-order form,

$$\begin{aligned} & \ddot{K} + 2\zeta\omega_n \dot{K} + \omega_n^2 K = 0 \\ & K = k - k_c \\ & \zeta\omega_n = \frac{\nu_L}{r_c^2 \ln \frac{r_\infty}{r_c}} \end{aligned} \quad (2.12)$$

$$f_n = \frac{\omega_n}{2\pi} = \frac{U_\infty}{2\pi r_c} \sqrt{\frac{\sigma}{\ln \frac{r_\infty}{r_c} \frac{1 + e^{-2ak_c^2} - 2e^{-ak_c^2}}{1 + e^{-2ak_c^2} - 2e^{-ak_c^2} + 2ak_c^2 Ei(-2ak_c^2) - 2ak_c^2 Ei(-ak_c^2)}}}$$

where K is the radial perturbation of R relative to r_{cv} , ζ is the damping ratio, and $\omega_n = 2\pi f_n$, represents the modified natural frequency.

Once f_n is calculated by the Equation (2.12), the tangential stiffness coefficient K_σ in the Equation (2.1) is updated to,

$$K_\sigma(k_c) = \frac{1 + e^{-2ak_c^2} - 2e^{-ak_c^2}}{1 + e^{-2ak_c^2} - 2e^{-ak_c^2} + 2ak_c^2 Ei(-2ak_c^2) - 2ak_c^2 Ei(-ak_c^2)} \quad (2.13)$$

Bosschers *et al.* (2018a) have pointed out the relations between cavitation inception number (σ_i) and $k_c = r_c/r_{cv}$. However, the onset of TVC is very sensitive to the nuclei of incoming flow, turbulence and scale effects (Zhang *et al.* 2015; Peng *et al.* 2017b), the desinent cavitation number (σ_d) is relatively stable and primarily influenced by the gas content (Arndt 2002; Song *et al.* 2017). Therefore, σ_d is more suitable to reflect the relationship rather than σ_i . The solution of σ_d is given by letting r_c approach the vortex axis in the radial direction,

$$\begin{aligned} \sigma_d &= (p_\infty - p(r_c)|_{r_c \rightarrow 0}) / \frac{1}{2} \rho_L U_\infty^2 \\ &\approx \frac{\Gamma_\infty^2}{4\pi^2 U_\infty^2 r_{cv}^2} \frac{1 + e^{-2ak_c^2} - 2e^{-ak_c^2} + 2ak_c^2 Ei(-2ak_c^2) - 2ak_c^2 Ei(-ak_c^2)}{k_c^2} \Big|_{k_c \rightarrow 0} = \frac{a \ln 2 \Gamma_\infty^2}{2\pi^2 U_\infty^2 r_{cv}^2} \end{aligned} \quad (2.14)$$

By combining the Equations (2.7) and (2.14), Γ_∞ can be eliminated, and the relative cavitation number, σ/σ_d , is obtained by,

$$\frac{\sigma}{\sigma_d} = \frac{1 + e^{-2ak_c^2} - 2e^{-ak_c^2} + 2ak_c^2 Ei(-2ak_c^2) - 2ak_c^2 Ei(-ak_c^2)}{2a \ln 2 k_c^2} \quad (2.15)$$

consequently, the tangential stiffness coefficient K_σ is completely determined by the Equation (2.13) with σ/σ_d .

The experimental data measured from the stereo particle image velocimetry (SPIV) and high-speed video (HSV) for angles of attack equaling to 5° , 7° and 9° is provided by Bosschers (2018b) and marked in figures 1(a), (b) and (c). The desinent cavitation number, σ_d is calculated by the Equation (2.14), where r_{cv} has been proven to be equal to the vortex core radius in non-cavitating flows, therefore measured as $1.00mm$, $1.15mm$ and $1.60mm$, respectively. Note that the blue curves bound the error variation of 10% or 15% from the averaged value of cavity radius r_{cv} . The results indicate that all experimental data are covered by the predicted band of r_c varying with σ , and the theoretical relation in the Equation (2.15) is verified.

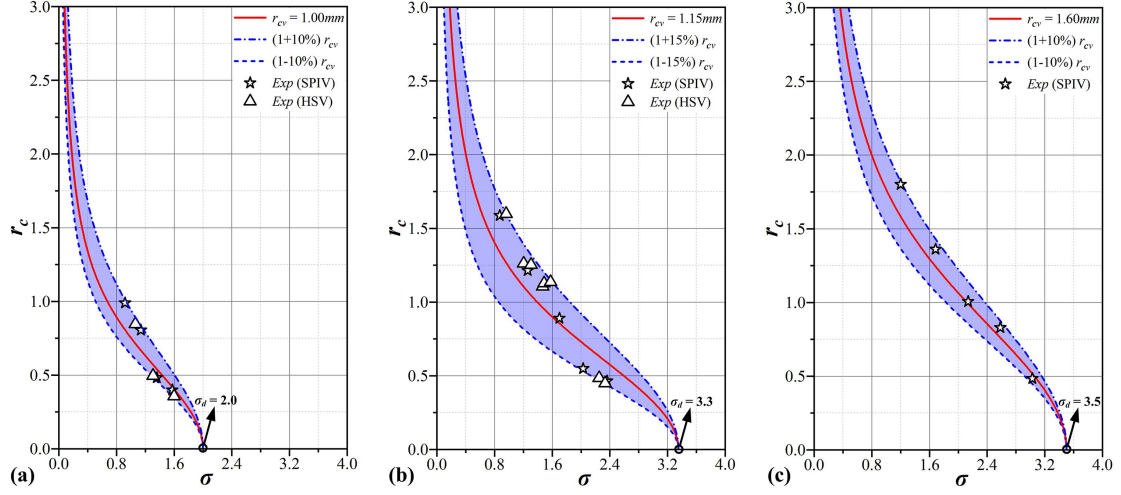


FIGURE 1. The measured cavity radius, r_c , varying with σ obtained by SPIV and HSV for the angles of attack at 5° , 7° and 9° , the theoretical curves are depicted using the Equation (2.15) for (a) $r_{cv} = 1.00\text{mm}$ (with 10% error band), $\sigma_d = 2.0$, (b) $r_{cv} = 1.15\text{mm}$ (with 15% error band), $\sigma_d = 3.3$, and (c) $r_{cv} = 1.60\text{mm}$ (with 10% error band), $\sigma_d = 3.5$.

Compared with semi-empirical models in Bosschers *et al.* (2018a), this approach contains no empirical parameters and provides an accurate fit of r_c with σ . Therefore, the bubble's natural frequency in the Equation (2.1) is updated to,

$$f_n = \frac{U_\infty}{2\pi r_c} \sqrt{\sigma K_\sigma (\sigma/\sigma_d) \left/ \ln \frac{r_\infty}{r_c} \right.} \quad (2.16)$$

Based on above discussions, for a step change in far-field pressure, f_n is believed to trigger the near-end TVC's resonance and singing if the incoming flow is properly changed to the singing condition. Note that although the Equation (2.16) has the same form as the Equation (2.1), K_σ is completely different: $K_\sigma = 1.0$ for the conventional method, and a function determined by σ/σ_d for the proposed method.

2.2. Dispersion relations for 3-D singing interfacial waves

The theoretical analysis of self-excited oscillations for a 2-D cavitation bubble focuses on the triggering at the far-end of TVC. However, the key to understanding vortex singing lies in how those disturbances propagate upstream and further excite the resonance of the near-end cavity. Therefore, to explain why such humming tone is triggered only in a narrow range of cavitation number, the 3-D dispersion relations describing the cavity interfacial dynamics are utilized. According to Bosschers *et al.* (2018b), particularly for small-scale axial phase velocity or low frequency oscillation, the non-dimensional dispersion relation is expressed as,

$$\tilde{\omega}^\pm(\kappa, k_\theta) = \frac{2\pi f^\pm r_c}{U_\infty} = \frac{U_c}{U_\infty} \kappa + \frac{V_c}{U_\infty} \left[k_\theta \pm \sqrt{\frac{-\kappa K'_{k_\theta}(\kappa)}{K_{k_\theta}(\kappa)}} \right] \quad (2.17)$$

here $\tilde{\omega}$ is the resonant frequency, $\kappa = k_x r_c = -ik_r r_c$ denotes the wavenumber, and k_θ is the azimuthal wavenumber. U_c and V_c respectively stand for the mean axial and

azimuthal velocities on the TVC surface, with K_{k_θ} referring to a modified *Bessel* function of the second kind (Bosschers 2008).

The plus and minus signs in the Equation (2.17) correspond to two frequencies of each cavity oscillation mode. And surface tension effects are deemed negligible for a small cavity core size (Pennings *et al.* 2015a). Here figure 2 illustrates the primary cavity oscillation modes,

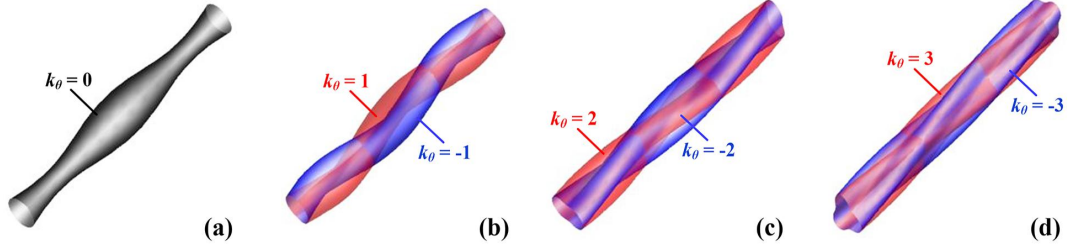


FIGURE 2. Shapes of cylindrical cavity oscillation modes for (a) monopole breathing mode at $k_\theta = 0$, (b) dipole centreline displacement mode at $k_\theta = \pm 1$, (c) quadrupole helical mode at $k_\theta = \pm 2$ and (d) hexapole helical mode at $k_\theta = \pm 3$.

Assuming $U_c/U_\infty = 1.0$ as per Bosschers (2008) due to the lack of analytical model for predicting U_c , we can derive the interfacial azimuthal velocity with the Bernoulli equation,

$$\frac{V_c}{U_\infty} = \sqrt{\frac{p_\infty - p_v}{0.5\rho_L U_\infty^2}} = \sigma^{0.5} \quad (2.18)$$

The distributions of $U_c = U_\infty$ and $V_c = \sigma^{0.5}U_\infty$ adhere to the potential vortex solution. For a stationary TVC per the viscous *Lamb-Oseen* model, V_c is replaced by the mean tangential velocity from Equation (2.4) when $r = r_c$, and Equation (2.18) becomes,

$$\frac{V_c}{U_\infty} = \frac{u_\theta(r_c)}{U_\infty} = \frac{\Gamma_\infty}{2\pi r_c U_\infty} [1 - e^{-a(r_c/r_\infty)^2}] \quad (2.19)$$

combining Equations (2.7), (2.13) and (2.15), the relation is further expressed as,

$$\frac{V_c}{U_\infty} = \sqrt{\sigma K_\sigma(\sigma/\sigma_d)} \quad (2.20)$$

To account for the axial acceleration effect induced by the reduction of tangential velocity, we apply the *Bernoulli* equation once more along the streamline developing from far-field to cavity surface, leading to,

$$\frac{U_c}{U_\infty} = \sqrt{\frac{p_\infty - p_v}{0.5\rho_L U_\infty^2} + 1 - \left(\frac{V_c}{U_\infty}\right)^2} = \sqrt{\sigma + 1 - \sigma K_\sigma(\sigma/\sigma_d)} \quad (2.21)$$

Thus, the non-dimensional dispersion relation in Equation (2.17) for 3-D singing waves is recalculated using Equations (2.20) and (2.21),

$$\tilde{\omega}^\pm(\kappa, k_\theta) = \kappa \sqrt{\sigma + 1 - \sigma K_\sigma(\sigma/\sigma_d)} + \sqrt{\sigma K_\sigma(\sigma/\sigma_d)} [k_\theta \pm \sqrt{\frac{-\kappa K'_{k_\theta}(\kappa)}{K_{k_\theta}(\kappa)}}] \quad (2.22)$$

The revised equation for 3-D resonance frequencies is solely dependent on σ and σ/σ_d according to the Equation (2.22). Compared to the assumption of $U_c/U_\infty = 1.0$ in Bosschers (2008), Equation (2.22) is believed to improve the accuracy of predicting the wavelength of interfacial waves.

To summarize the three schemes for predicting the interfacial waves, the ratios of the tangential velocity, V_c , and axial velocity, U_c , to the incoming velocity, U_∞ , are presented in table 1, where scheme *I* is the conventional model using the potential vortex assumption, scheme *II* is the revised model by incorporating the *Lamb-Oseen* vortex model and scheme *III* is the newly proposed model in the present study. It is clear that the theoretical analysis with scheme *III* needs no any empirical parameter, and should be promising for predicting the complicated TVC dynamics. In practice, both the Equations (2.16) and (2.22) are much improved for predicting the resonance frequencies of 2-D cavitation bubble oscillations and the dispersion of 3-D TVC interfacial waves by incorporating the dependency on σ/σ_d .

TABLE 1. Two velocity ratios determined by different models.

<i>Scheme</i>	<i>I</i>	<i>II</i>	<i>III</i>
V_c/U_∞	$\sigma^{0.5}$	$(\sigma K_\sigma)^{0.5}$	$(\sigma K_\sigma)^{0.5}$
U_c/U_∞	1.0	1.0	$(\sigma+1-\sigma K_\sigma)^{0.5}$

3. Results and discussions

3.1. Triggering for the vortex singing frequency

The experiment conducted by CSSRC, operating at conditions of $U_\infty = 7m/s$ and a dissolved oxygen level of $D_O = 68\%$, serves to validate the equations presented in section 2. According to Peng *et al.* (2017a), a twisted stationary TVC appears before singing, the noise levels abruptly intensify as the incoming pressure slowly increases until the cavitation number σ reaches 1.40. By maintaining the pressure, the vortex continues to singing for several seconds or minutes due to the presence of resembling standing waves along the cavity surface, ceasing only as the vibration decays. The primary frequency of vortex singing identified as $f_s = 320Hz$ on the noise spectrum, aligns precisely with the vibration frequency observed from the ‘dancing’ cavity. The desinent cavitation number for this test is given as $\sigma_d \approx 2.30$ (Song *et al.* 2017), resulting in $\sigma/\sigma_d = 0.61$. The solved f_n from Equation (2.16) is 319Hz, which closely matches the measured f_s in the experiment. Further analysis, based on the revised dispersion relation in the Equation (2.22), reveals a zero-group-velocity point ($\partial\omega/\partial\kappa = 0$) located on the breathing mode curve ($k_\theta = 0^\circ$), yielding the frequency of $f_{zgv} = 324Hz$, slightly larger than f_s . Although three frequencies f_s , f_n and f_{zgv} appear close quantitatively, their specific relationships require clearer elucidation.

The variations of cavity radius in time (t) and space (x), from two orthogonal views of the ‘dancing’ TVC, are recorded by the high-speed video and analyzed using Canny’s edge detection method (Canny 1986). As shown in figure 3(a), the xy plane view displays spindle-shaped radius contours distributed along the flow direction, representing helical waves with a fixed wavelength, $\lambda_s \approx 23.5mm$. Moreover, a laminar

zero frequency, representing a stationary wave, associated with a singing wavenumber measured as $\kappa_s = 2\pi r_c / \lambda_s = 0.348$. It is also clear that there are two oblique bright stripes indicating high-amplitude cavity radius oscillations. As figure 4(a) indicates, none of the dispersion curves predicted by *Scheme I* aligns with the high-amplitude region. The frequency at zero-group-velocity point i.e. f_{zgv} calculated by $\partial\tilde{\omega}/\partial\kappa = 0$ is plotted with the blue star mark, and is far away from the singing frequency, $\tilde{\omega}_s = -0.378$. For *Scheme II* as plotted in figure 4(b), two double helical modes i.e. $k_\theta = 2^-$ and $k_\theta = -2^+$ seem to approach the oblique bright stripes on the diagram within the first and fourth quadrants, with f_{zgv} locating somewhat closer to f_s . However, the dispersion curve of $k_\theta = -2^+$ still exhibits considerable deviation from the right oblique bright stripe. For the results of *Scheme III* in figure 4(c), the dispersion curves' slope shows a better fitting accuracy of the highlighted background, and f_{zgv} is much closer to f_s . The stationary wavenumber at the zero-frequency point, i.e. the wavenumber at the intersection of the dispersion curve of $k_\theta = -2^+$ and $\tilde{\omega} = 0$ is calculated as $\kappa_{zf} = 0.335$, which approaches the singing wavenumber κ_s . It is evident that *Scheme III* provides a more accurate representation of TVC dynamics under singing conditions compared to *Schemes I* and *II*.

From figure 4(c), it is noticed that the oscillation energy at the zero-group-velocity point manifests as a bright spot, located close to the intersection between dispersion curves of $k_\theta = -2^+$ and $k_\theta = 0^-$. However, further clarification is required to ascertain whether the most high-amplitude oscillation originates from the breathing mode of $k_\theta = 0^-$ or the double helical mode of $k_\theta = -2^+$.

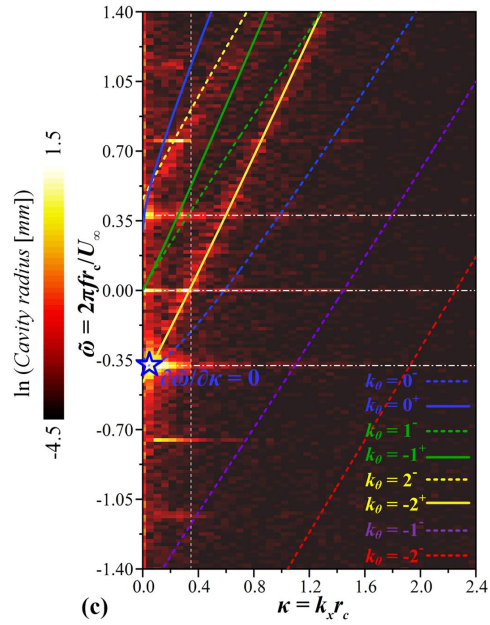
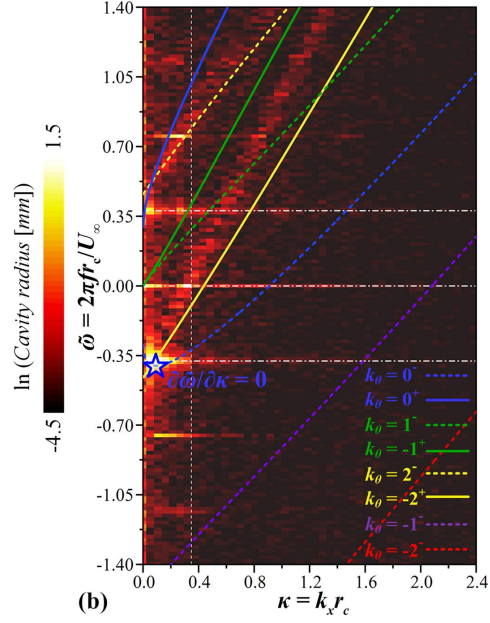
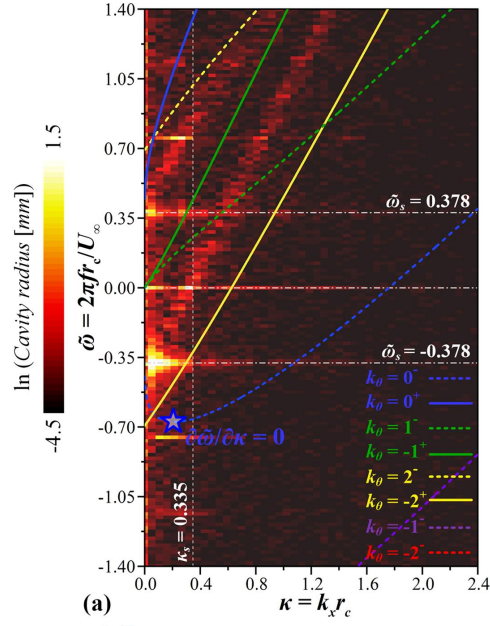


FIGURE 4. Frequency-wavenumber diagram of the variation of cavity radius on the xy plane at the singing condition ($\sigma_s = 1.40$, $\sigma_d \approx 2.30$) from *CSSRC*, the dispersion coefficients for comparison are obtained by (a) *Scheme I*, (b) *Scheme II* and (c) *Scheme III* (Iso colours indicate the cavity radius amplitude).

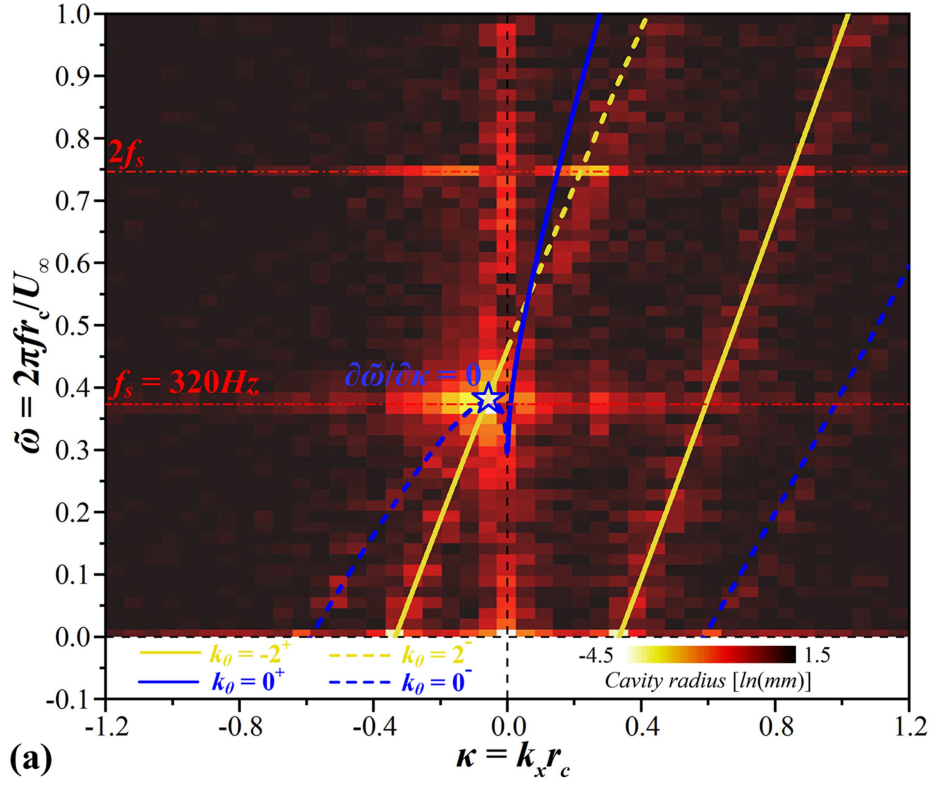
The frequency-wavenumber diagram from the xz plane view is illustrated in figure 5(a), where the first and second quadrants are plotted for validation according to the symmetry. Through *Scheme III*, the predicted dispersion curves match with the bright oblique stripes on the background, especially for the double helical waves of $k_\theta = 2^-$ and $k_\theta = -2^+$, while some faint bright stripes are also derived near the breathing mode curve of $k_\theta = 0^-$.

For further analysis, the coherence between two camera views of the xy plane and xz plane is presented in decibel and valued by,

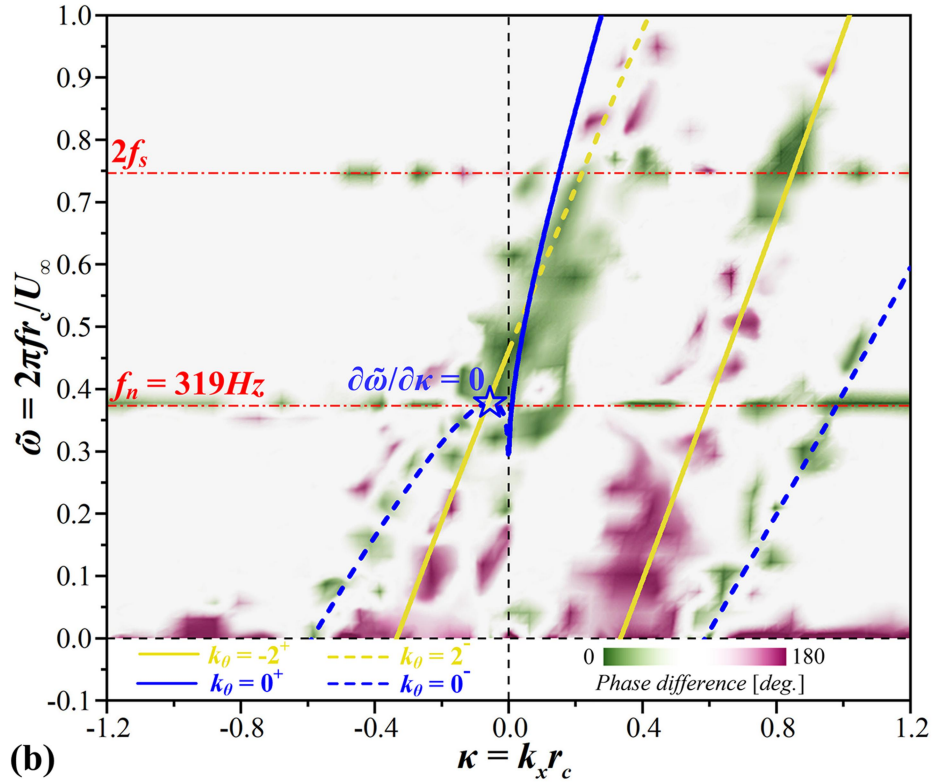
$$Coherence(k_x, f) = \frac{G_{xy}(k_x, f)G_{xz}^*(k_x, f)}{|G_{xy}(k_x, f)||G_{xz}(k_x, f)|} \quad (3.1)$$

where $G(k_x, f)$ is the 2-D FFT of cavity radius segments. The superscript, $*$, represents complex conjugation.

Using the Equation (3.1), the phase difference spectrum is plotted in figure 5(b). At the zero-frequency point, the phase difference of double helical mode ($k_\theta = -2^+$) is approaching 180° . As for the breathing mode curve of $k_\theta = 0^-$, the phase difference is close to 0° , as expected. Moreover, the phase difference near the zero-group-velocity point is basically close to 0° , confirming that f_{zgv} is stimulated by the breathing wave. However, from f_s to $2f_s$, the phase difference for the helical wave of $k_\theta = -2^+$ is also near 0° due to its proximity to the breathing mode curve of $k_\theta = 0^+$. To summarize, once the near-end TVC starts to sing by the disturbance from the far-end cavity, the cavity interfacial distortions should be mainly composed of double helical waves and breathing waves that are located near the zero-group-velocity point.



(a)



(b)

FIGURE 5. (a) Frequency-wavenumber diagram of cavity radius on the xz plane view at the singing condition ($\sigma_s = 1.40$, $\sigma_d \approx 2.30$) from CSSRC, the dispersion curves are obtained by Scheme III. (b) Phase difference between two camera views for the cavity radius.

To further reveal the triggering mechanism for a singing TVC, the cross-power spectral density (CPSD) of cavity radius variations from two orthogonal camera views is calculated by,

$$CPSD(k_x, f) = 120 + 10 \log_{10} \left\{ \frac{G_{xy}(k_x, f) G_{xz}^*(k_x, f)}{r_c^2} \right\} \quad (3.2)$$

As shown in figure 6(a), the local maxima of CPSD are concentrated firstly at the zero-group-velocity point on the breathing wave ($k_\theta = 0^-$) with frequency of f_{zgv} , and subsequently at the zero-frequency-point on the dispersion curves of $k_\theta = -2^+$ i.e. $f_{-2^+} = 0$. Under this condition, the frequency, f_i , at the intersection between the dispersion curves at $k_\theta = -2^+$ and $k_\theta = 0^-$, marked with the circle, is almost equal to f_{zgv} of 324Hz, indicating that the helical-shaped TVC starts to oscillate from a stationary state and then triggers f_{zgv} successfully through the far-end oscillation at $f_n = 319Hz$.

In figure 6(b), the wavenumbers at the zero-frequency point κ_{zf} and the zero-group-velocity-point κ_{zgv} are solved as -0.335 and -0.054, respectively. Thus, the wavelength at the zero-frequency point i.e. λ_{zf} is solved by $\lambda_{zf} = 2\pi r_c / \kappa_{zf} = -24.4mm$, and that at the zero-group-velocity-point i.e. λ_{zgv} is also determined as $\lambda_{zgv} = 2\pi r_c / \kappa_{zgv} = -151.3mm$. denoting the relation of $\lambda_{zgv} \approx 6.2\lambda_{zf}$ for these two wavelengths. Furthermore, the phase velocity at the zero-group-velocity-point i.e. V_{bw} , calculated by $f_{zgv}\lambda_{zgv}$, is -49.0m/s, which is the slope of the purple solid line in figure 6(b). Note that the negative sign of phase velocity implies a breathing wave travelling upstream.

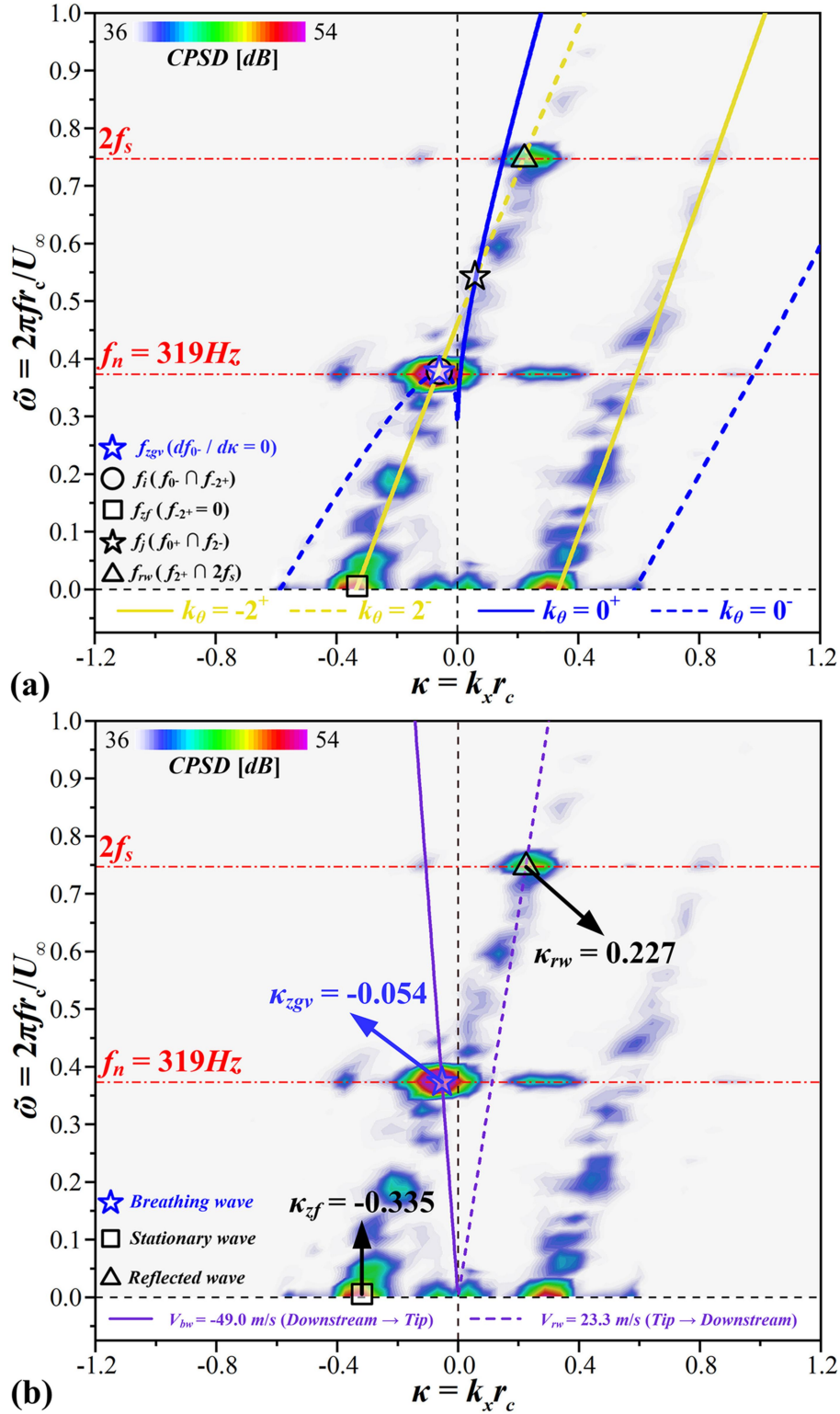


FIGURE 6. Frequency-wavenumber diagram of the cavity radius computed through CPSD at the singing condition ($\sigma_s = 1.40$, $\sigma_d \approx 2.30$) from CSSRC, with (a) theoretical feature points on dispersion curves deduced by Scheme III and (b) the phase velocity of breathing waves and reflected waves.

As figure 6(a) plots, there is also the region with a third highest amplitude of CPSD near the intersection between the line of $f_{rw} = 2f_s$ and the dispersion curve of $k_\theta = 2^-$.

The subscript rw stands for a ‘reflected wave’ moving downstream, the wavenumber κ_{rw} at the intersection is 0.227, and then the wavelength i.e. λ_{rw} is calculated by $\lambda_{rw} = 2\pi r_c / \kappa_{rw} = 36.0\text{mm}$. Furthermore, the phase velocity V_{rw} at the intersection is 23.3m/s calculated by $V_{rw} = 2f_s \lambda_{rw}$, which is the slope of the purple dash line in figures 6(b) and represents the speed of a downstream-propagating wave, implying that the breathing distortions seem to be basically absorbed by the sheet cavitation but generates limited reflected waves. Therefore, the oscillating LSC at the tip is not a ‘trigger’, as assumed by earlier studies, but more like a ‘muffler’, exerting little effect on the singing initiation but determining when the singing ends.

3.2. Insights into singing vortex dynamics

Except for the mean mode ($\tilde{\omega} = \kappa = 0$), waves at the zero-group-velocity and the zero-frequency points exhibit the two largest amplitudes of cavity radius oscillation, as illustrated in figures 4 and 5. To simplify the representation of these singing waves under CSSRC’s condition ($\sigma_s = 1.40$, $\sigma_d \approx 2.30$), R_{zf} refers to the radius of helical wave ($k_\theta = -2^+$) at the zero-frequency point, the amplitude, frequency and wavelength are A_{zf} , f_{zf} and λ_{zf} , respectively. R_{zgv} is the radius of a breathing mode wave ($k_\theta = 0^-$) at the zero-group-velocity point, where the magnitude, frequency and wavelength are A_{zgv} , f_{zgv} and λ_{zgv} respectively. These parameters, in both two camera views for xy and xz planes are presented in figure 3, and given in table 2. It is evident that the wave amplitude at the zero-group-velocity, A_{zgv} , is larger than that at the zero-frequency point, A_{zf} , and the wavelength at the zero-group-velocity, λ_{zgv} , is much longer than that at the zero-frequency point, λ_{zf} , i.e. $\lambda_{zgv} \approx 6.2\lambda_{zf}$, as indicated before.

TABLE 2. The parameters applied for simplifying singing waves at the singing condition ($\sigma_s = 1.40$, $\sigma_d \approx 2.30$) from (1) the xy plane view and (2) the xz plane view.

<i>Parameters</i>	A_{zf} [mm]	f_{zf} [Hz]	λ_{zf} [mm]	A_{zgv} [mm]	f_{zgv} [Hz]	λ_{zgv} [mm]
(1) xz plane	0.19	0	24.4	0.32	324	151.3
(2) xy plane	0.21			0.36		

To analyze features of a singing TVC, a synthetic wave R_{zf+zgv} is constructed based on R_{zf} and R_{zgv} , which represent two waves with the first two largest amplitudes of the cavity radius oscillation. Given the equilibrium radius of cavity, $r_c = 1.30\text{mm}$, the singing waves can be expressed as,

$$\begin{cases} R_{zf}(x, \theta, t) = r_c + A_{zf} \exp\left\{i\left(\frac{-2\pi x}{\lambda_{zf}} - 2\theta + 2\pi f_{zf} t\right)\right\} \\ R_{zgv}(x, \theta, t) = r_c + A_{zgv} \exp\left\{i\left(\frac{-2\pi x}{\lambda_{zgv}} + 2\pi f_{zgv} t\right)\right\} \\ R_{zf+zgv}(x, \theta, t) = r_c + A_{zgv} \exp\left\{i\left(\frac{-2\pi x}{\lambda_{zgv}} + 2\pi f_{zgv} t\right)\right\} + A_{zf} \exp\left\{i\left(\frac{-2\pi x}{\lambda_{zf}} - 2\theta + 2\pi f_{zf} t\right)\right\} \end{cases} \quad (3.3)$$

To validate this approach, we select four typical instants within the singing cycle. In figure 7, the cavity from the top view (xz plane) of CSSRC’s tunnel, showcasing the

interfacial shapes with radii of R_{zf} , R_{zgv} and R_{zf+zgv} at each time instant. For each wave, the location with the maximum diameter is identified as the crest. The crest A , occurs at $x/C = 0.78$ for the time instant $t_0 = 0.010s$. Then, the crest A , carried by breathing waves, propagates upstream from $x/C = 0.78$ at t_0 to $x/C = 0.52$ at t_1 , which further approaches $x/C = 0.00$ at t_2 . At t_2 , the crest B is theoretically predicted at $x/C = 1.61$. The distance between these two crests (A and B) corresponds to λ_{zgv} , indicating that a large-scale volume pulsation is travelling along the singing TVC. By $t_3 = 0.012s$, crest B reaches $x/C = 1.35$ with V_{bw} of $-49.0m/s$. The simplified singing waves, shaped by R_{zf+zgv} , faithfully reproduce the experimental details of a ‘dancing’ cavity.

From t_2 to t_3 , both the upstream and downstream of the TVC undergo self-excited contraction and expansion, respectively. Guided by the traction-propulsion effect, the trough C i.e. the location with the minimum diameter for each wave, along the R_{zf+zgv} is forced to move upstream from $x/C = 0.72$ at t_2 to $x/C = 0.46$ at t_3 with the phase velocity of V_{bw} . Therefore, the 2-D self-excited oscillations, occurring with a natural frequency, $f_n = 319Hz$, as predicted by Equation (2.16), can trigger the wave at zero-group-velocity point and sustain 3-D breathing waves, which serve as the dominant source of vortex singing.

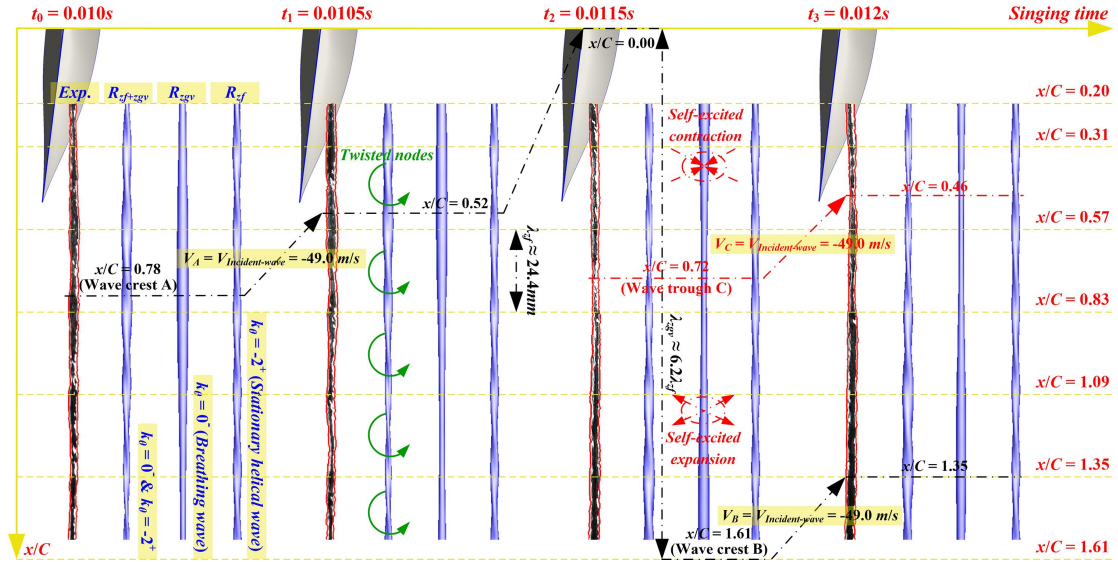


FIGURE 7. Four typical time instants within a singing cycle from the top view of CSSRC’s tunnel (xz plane), and the waves are simplified using the Equation (3.3) at the singing condition ($\sigma_s = 1.40$, $\sigma_d \approx 2.30$).

Considering the side view (xy plane) and utilizing the Equation (3.3), R_{zf} , R_{zgv} and R_{zf+zgv} are compared with experimental data in figure 8. The helical wave ($k_\theta = -2^+$) exhibits a 180° phase difference between two views, e.g. the intersection between the yellow location line and the shape of R_{zf} shifts from wave crests (maximum diameter) on the xz plane to wave nodes (minimum diameter) on the xy plane, and vice versa. Since there is no phase difference for breathing waves, the evolution of wave crests A and B , as well as the trough C on the R_{zgv} from t_0 to t_3 closely replicates that recorded from the top view. As figure 8 demonstrates, the synthetic wave R_{zf+zgv} captures the strong volume pulsation travelling along the twisted TVC, with $\lambda_{zgv} \approx 6.2\lambda_{zgf}$ keeping in

implies that $f_i = f_{zgv}$ is probably one of the singing criteria. By applying the Equation (2.22), the 3-D dimensionless resonance frequencies are given as,

$$\begin{cases} \tilde{\omega}^-(\kappa, 0) = \frac{2\pi f_0 r_c}{U_\infty} = \kappa \sqrt{\sigma + 1 - \sigma K_\sigma(\sigma/\sigma_d)} - \sqrt{\sigma K_\sigma(\sigma/\sigma_d)} \sqrt{\frac{-|\kappa| K'_0(|\kappa|)}{K_0(|\kappa|)}} \\ \tilde{\omega}^+(\kappa, -2) = \frac{2\pi f_{-2^+} r_c}{U_\infty} = \kappa \sqrt{\sigma + 1 - \sigma K_\sigma(\sigma/\sigma_d)} + \sqrt{\sigma K_\sigma(\sigma/\sigma_d)} \left\{ -2 + \sqrt{\frac{-|\kappa| K'_2(|\kappa|)}{K_2(|\kappa|)}} \right\} \end{cases} \quad (3.4)$$

here, if $\kappa > 0$, the wavenumber at the intersection κ_i can be solved from the relation $\tilde{\omega}^-(\kappa, 0) = \tilde{\omega}^+(\kappa, -2)$, yielding $\kappa_i = 0.062$.

The singing criterion can be derived at the extremum by,

$$\left. \frac{\partial \tilde{\omega}^-(\kappa, 0)}{\partial \kappa} \right|_{\kappa=\kappa_i} = \sqrt{\sigma + 1 - \sigma K_\sigma} - \frac{\sqrt{\sigma K_\sigma}}{2|\kappa_i|} \sqrt{\frac{-|\kappa_i| K'_0(|\kappa_i|)}{K_0(|\kappa_i|)}} \left\{ 1 + \frac{|\kappa_i| K'_0(|\kappa_i|)}{K'_0(|\kappa_i|)} - \frac{|\kappa_i| K'_0(|\kappa_i|)}{K_0(|\kappa_i|)} \right\} = 0 \quad (3.5)$$

by applying $\kappa_i = 0.062$, the following analytical relation can be achieved,

$$1 + \frac{1}{\sigma} = 3.445 K_\sigma(\sigma/\sigma_d) \quad (3.6)$$

For convenience, the relation shown by Equation (3.6) is termed the first singing-line- a , representing one of triggering mechanisms for TVC-singing. As illustrated by Equations (2.13) and (2.15), K_σ is solely dependent on σ/σ_d . Therefore, for each σ/σ_d , the theoretical singing cavitation number satisfying the Equation (3.6) can be defined, and the singing frequency within the second quadrant, $\tilde{\omega}^a$, is predicted using either of the Equations provided in (3.4),

$$\tilde{\omega}^a(\sigma/\sigma_d) = -\tilde{\omega}^-(\kappa_i, 0) = 0.488 \sqrt{\frac{K_\sigma}{3.445 K_\sigma - 1}} \quad (3.7)$$

as σ_d varies, the first singing-line- a is plotted by the blue curve in figure 9(a). Once σ_d reaches 1.64, the curves with frequencies of f_i and f_{zgv} have the intersect at $\sigma/\sigma_d = 0.35$ marked with Triggered point-A, indicating that TVC-singing can only be triggered at the cavitation number of $\sigma = 0.35 \times 1.64 = 0.57$.

In figure 9(b), the ‘dancing’ cavity is expected to disperse along the curve at $k_\theta = -2^+$ and further stimulate the zero-group-velocity point with $\tilde{\omega} = 0.32$, allowing f_{zgv} to be fully triggered through f_i at the intersection.

However, as σ_d increases, there are two solutions, $\kappa = -0.062$ and $\kappa = 0.062$, of $\sigma/\sigma_d = 0.35$, which satisfies the criterion $f_i = f_{zgv}$. According to Equations (3.6), (2.13) and (2.15), as σ/σ_d approaches 0, then k_c will approach ∞ and K_σ will approach 1, resulting in $\sigma = 0.41$, which represents the minimum cavitation number for triggering vortex singing. Furthermore, if σ is large enough, K_σ approaches 0.29 and the solution of the Equation (3.6) is $\sigma/\sigma_d = 0.73$, where the asymptotic-line- a is located in figure 9(a).

For $k_\theta = -0^+$ and $k_\theta = 2^-$, dimensionless frequencies are derived from the Equation (2.22), i.e.

$$\left\{ \begin{array}{l} \tilde{\omega}^+(\kappa, 0) = \frac{2\pi f_{0^+} r_c}{U_\infty} = \kappa \sqrt{\sigma + 1 - \sigma K_\sigma(\sigma/\sigma_d)} + \sqrt{\sigma K_\sigma(\sigma/\sigma_d)} \sqrt{\frac{-|\kappa| K'_0(|\kappa|)}{K_0(|\kappa|)}} \\ \tilde{\omega}^-(\kappa, 2) = \frac{2\pi f_{2^-} r_c}{U_\infty} = \kappa \sqrt{\sigma + 1 - \sigma K_\sigma(\sigma/\sigma_d)} + \sqrt{\sigma K_\sigma(\sigma/\sigma_d)} \left(2 - \sqrt{\frac{-|\kappa| K'_2(|\kappa|)}{K_2(|\kappa|)}} \right) \end{array} \right. \quad (3.8)$$

if $\kappa > 0$, a constant of $\kappa_j = 0.062$ is the solution to $\tilde{\omega}^+(\kappa, 0) = \tilde{\omega}^-(\kappa, 2)$. Solved from $\partial\tilde{\omega}^-/\partial\kappa = 0$, $\kappa_{zgv}(\sigma, K_\sigma)$ can be obtained as -0.38, inducing the singing tone at the zero-group-velocity point at $\tilde{\omega} = 1.03$. Therefore, the second singing criterion is,

$$\tilde{\omega}^-(\kappa_j, 2) = \tilde{\omega}^-(\kappa_{zgv}, 0) \quad (3.9)$$

As depicted in figure 10(a), if σ_d increases continuing, the criterion of $f_j = f_{zgv}$ starts to present two solutions locating at both sides of $\sigma/\sigma_d = 0.23$. These triggered points marked with circle symbol all behave in the second type and are further connected to the singing-line-*b*, shown as a red curve in figure 10(a) and satisfying the following relationship,

$$1 + \frac{1}{\sigma} = 1.422 K_\sigma(\sigma/\sigma_d) \quad (3.10)$$

Similarly, if σ/σ_d approaches 0, the minimum cavitation number can be calculated, i.e. $\sigma = 2.37$. when σ increases, σ/σ_d approaches 0.41, where the asymptotic-line-*b* is obtained, as shown in figure 10(a). And the frequency $\tilde{\omega}^b$ is computed using either of formulas in Equations (3.8), e.g.

$$\tilde{\omega}^b(\sigma/\sigma_d) = \tilde{\omega}^-(\kappa_j, 2) = 0.625 \sqrt{\frac{K_\sigma}{1.422 K_\sigma - 1}} \quad (3.11)$$

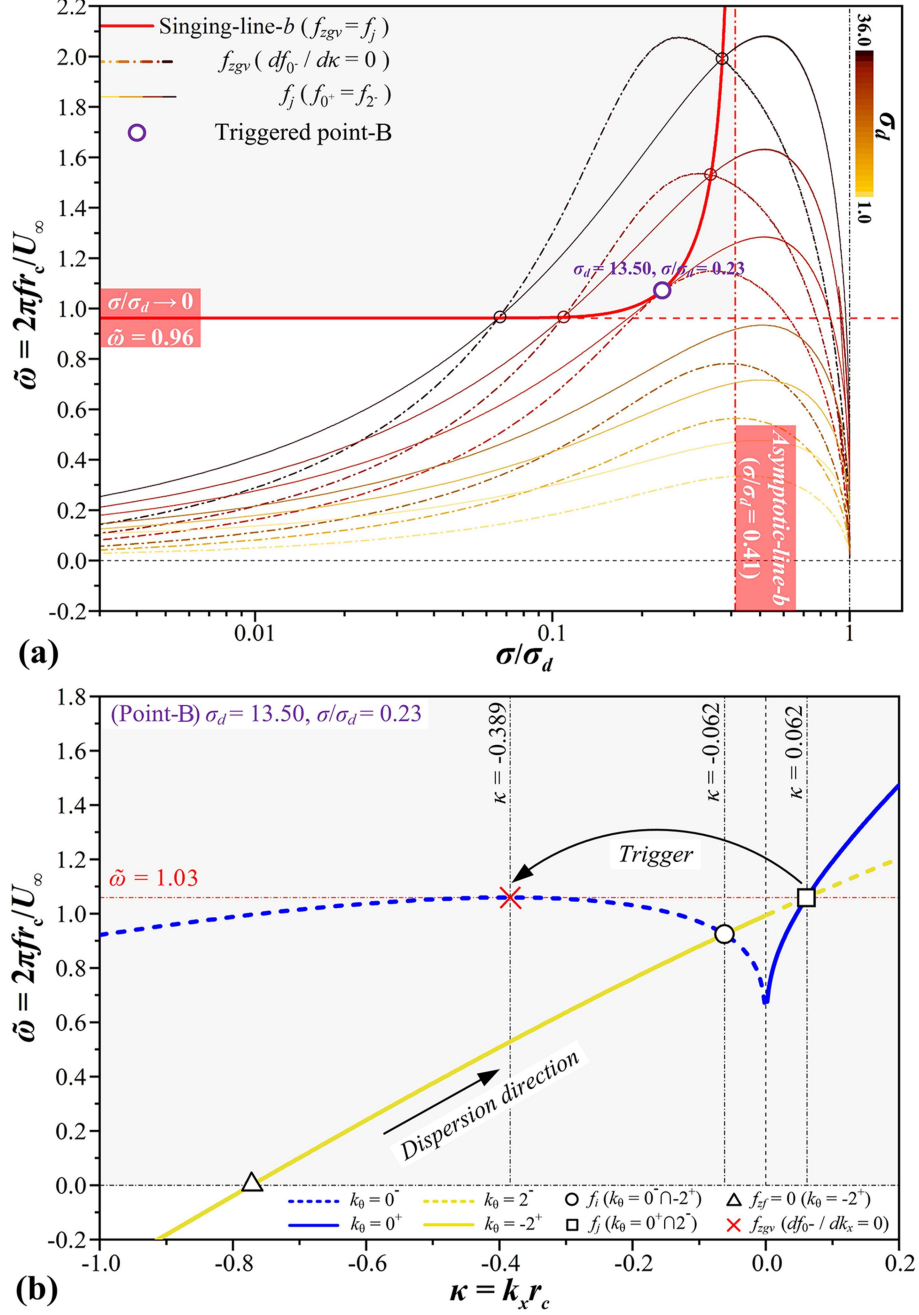


FIGURE 10. Second type of vortex singing triggering, (a) theoretical solution for the frequency of upper singing-line-*b* varying with σ/σ_d , (b) second trigger mechanism at point B ($\sigma_d = 13.50$, $\sigma/\sigma_d = 0.23$).

To validate the two vortex singing lines, the dataset provided by *CSSRC* and *G.T.H.* is used for comparison on the diagram of $(\sigma^{0.5}, \tilde{\omega})$ as shown in figure 11. Note that the available cavity radius measured by *G.T.H.* is simply treated as r_c . For the singing-line *a* representing the first criterion for the singing TVC, its non-dimensional frequency i.e. $\tilde{\omega}^a$ can be predicted by the relation of $\tilde{\omega}^a(\sigma) = 0.263 (\sigma+1)^{0.5}$, which is obtained by combining the Equations (3.10) and (3.11). For the singing-line-*b* representing the second criterion for the singing TVC, its non-dimensional frequency i.e. $\tilde{\omega}^b$ can be predicted by the relation of $\tilde{\omega}^b(\sigma) = 0.524 (\sigma+1)^{0.5}$. The relations are described by two

color solid lines, blue for the singing-line-*a*, and red for the singing-line-*b*.

As shown in figure 11, three sets of singing conditions in *CSSRC* under different dissolved oxygen contents are concentrated on singing-line-*a* and in the cavitation number range between $\sigma_{limit-a} = 0.41$ and $\sigma_{limit-b} = 2.37$. Here *A* and *B* represent the intersection points of $f_i \sim \sigma^{0.5}$ connecting $f_{zgv} \sim \sigma^{0.5}$ and $f_j \sim \sigma^{0.5}$ connecting $f_{zgv} \sim \sigma^{0.5}$, which are solved by the potential flow assumption and plotted with purple lines in figure 11. It is clear that in the case of $\sigma_{limit-a} \leq \sigma \leq \sigma_{limit-b}$, e.g. the singing region in *CSSRC*, the vortex singing can only be triggered along the singing-line-*a*. For the case of $\sigma > \sigma_{limit-b}$, e.g. four singing conditions in *G.T.H.*, the vortex singing is triggered along the singing-line-*b*.

In summary, we have presented and validated two theoretical vortex singing lines and explained why vortex singing can only occur within a narrow cavitation number range. This analysis provides insights into the underlying mechanisms governing the vortex singing and highlights the importance of hydrodynamic triggering conditions for such a whistling vortex cavity.

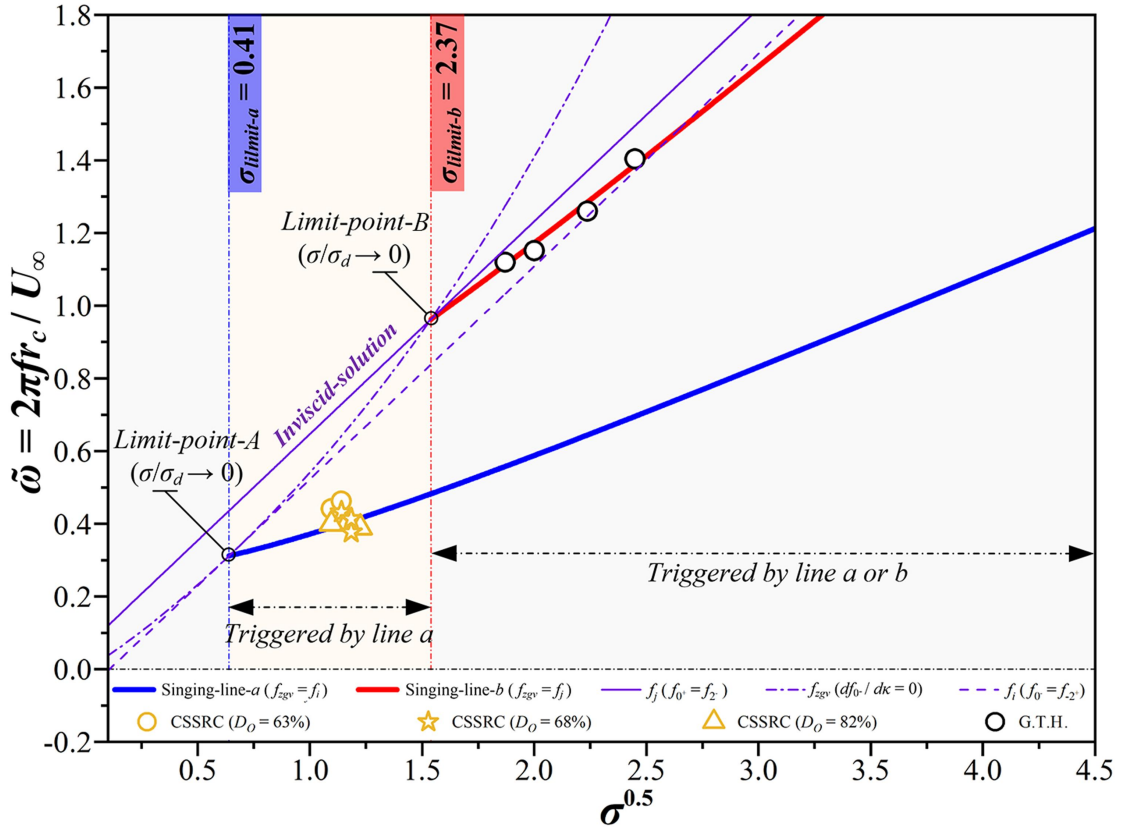


FIGURE 11. Theoretical solutions for the frequency of two vortex singing lines varying with $\sigma^{0.5}$, with singing conditions from *CSSRC* and *G.T.H.*

4. Conclusions

The phenomenon of vortex singing, a typical noise enhancement induced by the severe interfacial instability in tip vortex cavitating flows, has posed a significant challenge in cavitation hydrodynamic research over the past three decades. In this paper, theoretical analytical methods for predicting the 2-D resonance frequency of cavitation bubbles and the 3-D resonance frequency of cavity interfacial waves have

been proposed without involving any empirical parameters.

(1) To accurately predict the resonance frequency of TVC, the equation for 2-D resonance frequency i.e. f_n is established by introducing the *Lamb-Oseen* vortex model as well as the desinent cavitation number i.e. σ_d to linearize the 2-D viscous cavitation bubble's dynamic equation, the dispersion model of 3-D cavity interfacial waves is improved by further updating the tangential and axial cavity interfacial velocity based on the *Bernoulli* equation.

(2) The wavenumber-frequency spectrum of the singing cavity radius, derived from the experiment by *CSSRC*, is convincingly replicated by the proposed 3-D dispersion model, indicating that singing waves predominantly consist of the stationary double helical mode ($k_\theta = 2^-$ and -2^+) and the breathing mode ($k_\theta = 0^-$), rather than standing waves, as assumed in previous literatures. It is also confirmed that far-end oscillations at f_n play a crucial role in generating near-end breathing waves.

(3) Two trigger mechanisms have been proposed: The twisted TVC, initially at rest, is driven into motion by f_n due to a step change of the far-field pressure. Subsequently, the frequency associated with the zero-group-velocity point (f_{zgv}) at $k_\theta = 0^-$ is excited through f_i , the frequency at the intersection of dispersion curves at $k_\theta = 0^-$ and -2^+ , or f_j , the frequency at the intersection of dispersion curves at $k_\theta = 0^-$ and 2^- , corresponding to the first and second type of triggering approach for vortex singing, respectively.

(4) By applying the cavitation number (σ) and relative cavitation number (σ/σ_d), solutions for vortex singing frequency (f_s) are determined independently for two type of trigger mechanisms, and are expressed by two triggering lines, which are validated by singing cases in *CSSRC* and *G.T.H.*, respectively.

(5) Analysis based on the coherence and the cross-power spectral density of cavity radius oscillation between two camera views for singing TVC depicts a negative and large phase velocity, indicating a large-scale breathing mode wave propagating along the cavity surface and travelling from downstream towards the hydrofoil tip.

Acknowledgements: This work was supported by the National Natural Science Foundation of China (Nos. [52336001](#), [52309117](#)), and the China Postdoctoral Science Foundation (No: [2023M731895](#)). The authors would like to acknowledge professor Y. Q. Liu from Shanghai Jiao Tong University and professor Q. Q. Ye from Zhejiang University for their contributions in the analytical study.

Declaration of interests: The authors report no conflict of interest.

REFERENCES

- AMINI, A., RECLARI, M., SANO, T., LINO, M., DREYER, M. & FARHAT, M. 2019 On the physical mechanism of tip vortex cavitation hysteresis. *Exp. Fluids* **60** (7), 1-15.
- ARNDT, R. E. A., ARAKERI, V. H. & HIGUCHI, H. 1991 Some observations of tip-vortex cavitation. *J. Fluid Mech.* **229**, 269-289.
- ARNDT, R. E. A. & KELLER, A. P. 1992 Water quality effects on cavitation inception in a trailing vortex. *J. Fluids Eng.* **114**, 430-438.
- ARNDT, R. E. A. 2002 Cavitation in vortical flows. *Annu. Rev. Fluid Mech.* **34** (1), 143-175.

- ARNDT, R. E. A., PENNINGS, P. C., BOSSCHERS, J. & VAN TERWISGA, T. J. C. 2015 The singing vortex. *Interface focus* **5** (5), 20150025.
- ASNAGHI, A., SVENNERBERG, U., GUSTAFSSON, R. & BENSOW, R. E. 2020 Investigations of tip vortex mitigation by using roughness. *Phys. Fluids* **32** (6), 065111.
- BOSSCHERS, J. 2008 Analysis of inertial waves on inviscid cavitating vortices in relation to low-frequency radiated noise. In *Proceedings of the Warwick Innovative Manufacturing Research Centre (WIMRC) Cavitation: Turbo-machinery and Medical Applications Forum, Warwick University (UK)*.
- BOSSCHERS, J. 2009a Investigation of the resonance frequency of a cavitating vortex. In *Proceedings of the NAG/DAGA International Conference on Acoustics, Rotterdam, The Netherlands*.
- BOSSCHERS, J. 2009b Modeling and analysis of a cavitating vortex in 2D unsteady viscous flow. In *7th International Symposium on Cavitation CAV2009, Michigan, USA*.
- BOSSCHERS, J. 2018a An analytical and semi-empirical model for the viscous flow around a vortex cavity. *Int. J. Multiph. Flow* **105**, 122-133.
- BOSSCHERS, J. 2018b Propeller Tip-Vortex Cavitation and its Broadband Noise. PhD thesis, Delft University of Technology, Delft, The Netherlands.
- BRENNEN, C. E. 2014 Cavitation and bubble dynamics. *Cambridge university press*.
- BRIANÇON-MARJOLLET, L. & MERLE, L. 1997 Inception, development and noise of a tip vortex cavitation. In *Proceedings of the 21st Symposium on Naval Hydrodynamics, Trondheim, Norway*.
- CANNY, J. 1986 A computational approach to edge detection. *IEEE Trans. Pattern Anal. Mach. Intell.* **8** (6), 679-698.
- CHEN, L. Y., ZHANG, L. X., PENG, X. X. & SHAO, X. M. 2019 Influence of water quality on the tip vortex cavitation inception. *Phys. Fluids* **31** (2), 023303.
- CHENG, H. Y., LONG, X. P., JI, B., PENG, X. X. & FARHAT, M. 2021 A new Euler-Lagrangian cavitation model for tip-vortex cavitation with the effect of non-condensable gas. *Int. J. Multiph. Flow* **134**, 103441.
- CHOI, J. & CECCIO, S. L. 2007 Dynamics and noise emission of vortex cavitation bubbles. *J. Fluid Mech.* **575**, 1-26.
- CHOI, J., HSIAO, C.-T., CHAHINE, G. & CECCIO, S. 2009 Growth, oscillation and collapse of vortex cavitation bubbles. *J. Fluid Mech.* **624**, 255-279.
- FRANC J. P. & MICHEL J. M. 2006 Fundamentals of cavitation. *Springer science & Business media*.
- HIGUCHI, H., ARNDT, R. E. A. & ROGERS, M. F. 1989 Characteristics of tip vortex cavitation noise. *J. Fluids Eng* **111**, 495-501.
- JI, B., WANG, X. C., BAI, X., R., CHENG, H. Y. & PENG, X. X. 2023 Cavitation inception noise excited by a tip leakage vortex with various gap sizes: A Eulerian-Lagrangian investigation. *Phys. Fluids* **35** (12), 122107.
- KELLER, J. J. & ESCUDIER, M. P. 1980 Theory and observations of waves on hollow-core vortices. *J. Fluid Mech.* **99** (3), 495-511.
- KLAPWIJK, M., LLOYD, T., VAZ, G., BOOGAARD, M. V. D. & TERWISGA, T. V. 2022 Exciting a cavitating tip vortex with synthetic inflow turbulence: A CFD analysis of vortex kinematics, dynamics and sound generation. *Ocean Eng.* **254**, 111246.

- LIU, Y. Q. & WANG, B. L. 2019 Dynamics and surface stability of a cylindrical cavitation bubble in a rectilinear vortex. *J. Fluid Mech.* **865**, 963-992.
- LUO, X. W., QIAN, Z. H., WANG, X. C. & YU, A. 2022 Mode vortex and turbulence in ventilated cavitation over hydrofoils. *Int. J. Multiph. Flow* **157**, 104252.
- MAINES, B. & ARNDT, R. E. A. 1997 The case of the singing vortex. *J. Fluids Eng.* **119** (2), 271-276.
- PENG, X. X., WANG, B. L., LI, H. Y., XU, L. H. & SONG, M. T. 2017a Generation of abnormal acoustic noise: Singing of a cavitating tip vortex. *Phys. Rev. Fluids* **2** (5), 053602.
- PENG, X. X., XU, L. H., LIU, Y. W., ZHANG, G. P., CAO, Y. T., HONG, F. W. & YAN, K. 2017b Experimental measurement of tip vortex flow field with/without cavitation in an elliptic hydrofoil. *J. Hydrodyn.* **29** (6), 939-953.
- PENNINGS, P. C., BOSSCHERS, J., WESTERWEEL, J. & VAN TERWISGA, T. J. C. 2015a Dynamics of isolated vortex cavitation. *J. Fluid Mech.* **778**, 288-313.
- PENNINGS, P. C., WESTERWEEL, J. & VAN TERWISGA, T. J. C. 2015b Flow field measurement around vortex cavitation. *Exp. Fluids* **56** (11), 1-13.
- PENNINGS, P. C., WESTERWEEL, J. & VAN TERWISGA, T. J. C. 2016a Cavitation tunnel analysis of radiated sound from the resonance of a propeller tip vortex cavity. *Int. J. Multiph. Flow* **83**, 1-11.
- PENNINGS, P. C. 2016b Dynamics of Vortex Cavitation. PhD thesis, Delft University of Technology, Delft, The Netherlands.
- POSA, A., BROGLIA, R., FELLI, M., CIANFERRA, M. & ARMENIO, V. 2022 Hydroacoustic analysis of a marine propeller using large-eddy simulation and acoustic analogy. *J. Fluid Mech.* **947**, A46.
- QIAN, Z. H., WANG, Z., GENG, C. & LUO, X. W. 2022 Vortex and cavity dynamics for the tip-leakage cavitation over a hydrofoil. *Phys. Fluids* **34** (9), 093303.
- RUSSELL, P. S., BARBACA, L., VENNING, J. A., PEARCE, B. W. & BRANDNER, P. A. 2023 Influence of nucleation on cavitation inception in tip leakage flows. *Phys. Fluids* **35** (1), 013341.
- SIMANTO, R. I. A., HONG, J. W., AHN, B. K. & JEONG, S. W. 2023 Experimental investigation on tip vortex cavity deformation and flow dynamics using high-speed imaging and laser Doppler velocimetry measurements. *Phys. Fluids* **35** (10), 107104.
- SONG, M. T., XU, L. H., PENG, X. X. & TANG D. H. 2017 An acoustic approach to determine tip vortex cavitation inception for an elliptical hydrofoil considering nuclei-seeding. *Int. J. Multiph. Flow* **90**, 79-87.
- SONG, M. T., XU, L. H., PENG, X. X., TANG D. H. & CHEN, Y. H. 2018 Acoustic modeling of the singing vortex and its sound signatures. *Int. J. Multiph. Flow* **99**, 205-212.
- WANG, X. C., BAI, X. R., CHENG, H. Y., JI, B. & PENG, X. X. 2023 Numerical investigation of cavitating tip vortex dynamics and how they influence the acoustic characteristics. *Phys. Fluids* **35** (6), 062119.
- XIE, C. M., LIU, J. Y., JIANG, J. W. & HUANG, W. X. 2021 Numerical study on wetted and cavitating tip-vortical flows around an elliptical hydrofoil: Interplay of cavitation, vortices, and turbulence. *Phys. Fluids* **33** (9), 093316.
- YE, Q. Q., WANG, Y. W., WANG, Y. Q. & SHAO X. M. 2021 Dynamics and flow field of tip vortex cavitation. In *The 16th National Congress on Hydrodynamics & the 32nd*

- National Conference on Hydrodynamics, Wuxi, China.*
- YE, Q. Q., WANG, Y. W. & SHAO X. M. 2023 Dynamics of cavitating tip vortex. *Journal of Fluid Mechanics*, 2023, *J. Fluid Mech.* **967**, A30.
- ZHANG, L. X., ZHANG, N., PENG, X. X., WANG, B. L. & SHAO, X. M. 2015 A review of studies of mechanism and prediction of tip vortex cavitation inception. *J. Hydrodyn.* **27** (4), 488-495.